VILNIUS UNIVERSITY

CENTER FOR PHYSICAL SCIENCE AND TECHNOLOGY

TOMAS GRIGAITIS

INFLUENCE OF DOPOING ON THE OPTICAL AND ELECTRICAL PROPERTIES OF SIN_X FILMS DEPOSITED USING CVD TECHNOLOGY

SUMMARY OF DOCTORAL DISSERTATION

TECHNOLOGICAL SCIENCES, MATERIALS ENGINEERING (08 T)

VILNIUS, 2017

The research has been carried out in 2010–2016 at the Department of Solid State Electronics, Vilnius University.

Scientific supervisor:

prof. Dr. Kęstutis Arlauskas (Vilnius University, Technological Sciences, Materials Engineering – 08T).

Thesis consultant: dr. Kristijonas Genevičius (Vilnius University, Technological Sciences, Materials Engineering – 08T).

Doctoral thesis will be defended in the joint council of Vilnius University.

Chairman: prof. dr. Vincas Tamošiūnas (Vilnius University, Physical Sciences, Physics – 02 P).

Members:

dr. Renata Butkutė (Center for Physical Science and Technology, Technological Science, Materials Engineering – 08 T),

prof. Asta Guobienė (Kaunas University of Technology, Physical Science, Physics – 02 P),

habil. dr. Romualdas Navickas (Vilnius Gediminas Technical University, Technological Science, Materials Engineering – 08 T).

prof. dr. Ruud Schropp (Staff Utrecht University, Technological Science, Materials Engineering – 08 T).

The official defence of the doctoral thesis will be held in the public session of the Defence Council of Technological Science at 15 h on Febuary 13, 2017, in B306 room of National Centre of Physical and Technological Science, Saulėtekio al. 3, LT-10257 Vilnius, Lithuania.

The doctoral thesis is available at Vilnius University library and at the library of Center for Physical Sciences and Technology and also in the website of Vilnius University: www.vu.lt/lt/naujienos/ivykiu-kalendorius

VILNIAUS UNIVERSITETAS

KIETOJO KŪNO ELEKTRONIKOS KATEDRA

TOMAS GRIGAITIS

LEGIRAVIMO ĮTAKA CVD TECHNOLOGIJOS SiN_X:H SLUOKSNIŲ ELEKTRINĖMS IR OPTINĖMS SAVYBĖMS

Daktaro disertacijos santrauka,

Technologijos mokslai, medžiagų inžinerija (08 T)

Vilnius, 2017 metai

Disertacija rengta 2010 - 2016 metais, Vilniaus universitete, Kieto kūno elektronikos katedroje.

Mokslinis vadovas:

prof. dr. Kęstutis Arlauskas (Vilniaus Universitetas, technologijos mokslai, medžiagų inžinerija - 08T)

Mokslinis konsultantas: dr. Kristijonas Genevičius (Vilniaus universitetas, technologijos mokslai, medžiagų inžinerija – 08 T)

Disertacija ginama jungtinėje Vilniaus universiteto medžiagų inžinerijos krypties taryboje:

Pirmininkas: prof. dr. Vincas Tamošiūnas (Vilnius universitetas, fiziniai mokslai, fizika, 02 P).

Nariai:

Doc. dr. Renata Butkutė (Fizinių ir technologijos mokslų centras, technologijos mokslai, medžiagų inžinerija – 08 T),

prof. Asta Guobienė (Kauno technologijos universitetas, fiziniai mokslai, fizika – 02 P),

habil. dr. Romualdas Navickas (Vilniaus Gedimino technikos universitetas, technologijos mokslai, medžiagų inžinerija – 08 T).

prof. dr. Ruud Schropp (Staff Utrecht universitetas, technologijos mokslai, medžiagų inžinerija – 08 T).

Disertacija bus ginama viešame Medžiagų inžinerijos krypties tarybos posėdyje 2017 m. vasario 13 dieną 15 valandą Nacionalinio fizinių ir technologijos mokslų centro B336 auditorijoje, Saulėtekio al. 3, LT-10257 Vilnius, Lietuva.

Disertaciją galima peržiūrėti Vilniaus universiteto bibliotekoje ir VU interneto svetainėje adresu: www.vu.lt/lt/naujienos/ivykiu-kalendorius

Santrauka

Šiuo metu yra skiriamas didžiulis dėmesys silicio pagrindu veikiančių šviesos diodų kurimui ir tobulinimui, kuriuos ketinama panaudoti integriniuose grandynuose [1]. Eksperimentiškai yra pademonstruota tiek kristalinio, tiek porėtojo silicio ar silicio kvantinių darinių elektroliuminescencija (EL) [2, 3, 4], nors tokiu pagrindu suformuotos struktūros yra pakankamai sudėtingos, rezultatai sunkiai interpretuojami, o pagamintų įtaisų našumas netinkamas komercinei gamybai. Šiame darbe pristatoma sukonstruota trijų elektrodų plazminė cheminio garų nusodinimo kamera (PECVD) ir su ja suformuotų a-Si/SiN_x supergardelių ir Ce:SiN_x darinių EL, elektrinių ir morfologinių savybių analizė.

Šio darbo tikslas yra, naudojant trijų elektrodų PECVD įrangą, suformuoti optimalias SiN_x/a-Si:H nanometrinio storio sluoksnių elektroliuminescuojančias (EL) sandaras bei pagerinti jų EL savybes legiruojant Ceriu.

Disertacija sudaryta iš septynių skyrių, suskirstytų į poskyrius. Pirmas skyrius yra įvadinis, kuriame aptariami darbo tikslai ir uždaviniai, pristatomas darbo naujumas, ginamieji teiginiai, supažindinama su disertanto mokslinių straipsnių publikacijomis ir pranešimais konferencijoje.

Antrame skyriuje aprašoma silicio pagrindu EL struktūrų fizikiniai principai ir pagrindinės taikomos technologijos.

Trečioje dalyje pristatoma sukonstruota PECVD kamera ir SiN_x/a-Si:H bei Ce:SiN_x darinių formavimo principai bei pagrindiniai technologiniai parametrai.

Ketvirtoje dalyje aprašomi darbe taikyti tyrimo metodai.

Tyrimų rezultatai pristatomi penktame, šeštame ir septintame skyriuose. Šių skyrių rezulteatai aprašyti atitinkamai [S1], [S2] ir [S3] dabuose. Dviejų ir trijų elektrodų CVD kamerose pagamintų sluoksnių tyrimas ir jų palyginimas pristatomas penktame skyriuje. SiN_x/a-Si:H supergardelės bei Ce:SiN_x šviečiančių darinių struktūrinės, elektrinės ir optinės savybės pristatomos atitinkamai šeštame ir septintame skyriuose.

Introduction:

Huge efforts have been spent on developing high efficient Si-based light emitting devices (LEDs) which could be incorporated into c-Si based micro-electronic devices [1]. Many attempts have been made to turn Si into promising light emitting material focusing on porous silicon and various nano-size scale silicon structures [2, 3, 4].

Superlattice structures (SLs) of Si/SiN_x [5,6], Si/SiO_xN_y [7], SiN_x/SiN_y [8] and Si/SiO_2 [9] are investigated and SiN_x based superlattice is showing promising results for LED application due to the lower barrier height for both hole and electron injection into the active region compared to SiO_2 structures. The light emission is usually interpreted by either interfacial defect assisted radiative recombination or quantum confinement effect, however, the mechanism of electroluminescence (EL) is still under debate [10]. Although the influence of size of Si nanocrystallites, annealing conditions and the role of barrier layers to EL are investigated [8,11,12], however, the effect of altering the thickness of sublayers in a-Si:H/SiN_x SLs with high band gap of SiN_x with no post annealing still has not been properly explored.

Another technological alternative for the formation of Si-based LEDs is rare-earth (RE) doping. Doped silicon based lattices have attracted considerable attention due to the ability to emit the narrow wavelength radiation spectrum, low fabrication cost and compatibility with conventional silicon technology. Narrow spectrum of the emitted light usually arise due the electrons transition from 4f–4f orbitals which are partially shielded from the environment by the 5s and 5p orbitals. An efficient light-emitting devices based on various RE doped silicon structures have been demonstrated [13, 14, 15, 16]. On the other hand, usually the cerium silicates are formed with thermal annealing for up to 1200 °C and annealing at such high temperatures can cause film oxidation or incompatibility with temperature sensitive technologies.

In this work, we report our study of influence of various thickness sublayers to EL from a-Si:H/SiN_x SLs and we demonstrate the electroluminescence from the thin a-SiN_x films with embedded cerium atoms.

Work goals.

The aim of this work is to form electroluminescent SiNx/a-Si:H structures with optimal thickness of the sublayers and to deposit electroluminescent cerium doped SiN_x films.

Main objectoves:

1. To built the PECVD chamber, which would allow to control the deposition rate, width of the SiN_x band gap and other films properties.
2. To deposit a-Si:H/SiN_x SLs.
3. To determine the relationship between deposition parameters and the EL properties of the a-Si:H/SiN_x structures.
4. To deposit the electroluminescent Ce:SiNx films.
5. To determine the relationship between concentration of cerium and the EL properties of the Ce:SiN_x films.

Novelty:

This paper introduces the SiN_x, a-Si:H/SiN_x and Ce:SiN_x films's deposition technology, presents the optical, electrical and morphological properties of these films. The main novel results are:

1. It was shown that three electrode PECVD chamber is superior to the conventional parallel plate type reactor: additional electrode gives the ability to shift band gap of the SiN_x films in the wide range (1,85 eV – 5,15 eV), the layers have excellent electrical (ρ = 5,47 x 10^{14} Ωcm) and morphological (R_q = 3.9 nm) properties.
2. Presented the influence of various thickness sublayers of both a-Si:H and SiN_x to the EL from a-Si:H/SiN_x SLs.
3. Demonstrated the electroluminescence from thin a-SiN_x films with embedded cerium atoms.

Statements to defend:

1. Third electrode in the parallel plate PECVD reactor weakens the interaction between plasma and the depositing layer, therefore, this leads to the better morphological, electrical and optical properties of the films.
2. The main EL peak at ~700 nm is related to radiative recombination in thin a-Si:H layers and the peak at higher energy (~560 nm) is originated from a-Si:H/SiN_x interface defect states.
3. The broad emission band at 650 nm is originated from an optically active defects in Ce:SiN_x lattice and the 460 nm band is attributed to the radiative transition from 5d–4f energy levels of Ce^{3+} ions.

Layout of the thesis.

The thesis consists of seven chapters and reference list (163 titles). The text is written in Lithuanian language on 104 pages with illustrations presented in 43 figures and 3 tables. An introduction, main goals, statements to defend as well as the articles and conference presentations which concludes the presented data are listed at the **first chapter** of the thesis. The **second chapter** describes the main principles of silicon-based LEDs as well as the development and research history of Si-based LEDs. The sample preparation details and experimental techniques are described in the **third** and the **fourth chapter**, respectively. Original results are presented in chapters 5, 6 and 7**.** The results of the characterization of silicon nitride layers deposited in three-electrode PECVD chamber are demonstrated in **chapter 5**. The results of the electroluminescence from a-Si:H/SiN_x superlattice structures are showed in **chapter 6** and the **chapter 7** presents the results related to the electroluminescence from SiN_x layers doped with Ce^{3+} ions.

5. CHARACTERIZATION OF SILICON NITRIDE LAYERS [S1]

5.1 Experimental details

In the same two- and three-electrode deposition CVD chambers two series of samples were produced on both CaF_2 and on Al-coated glass substrates. The first series of samples (SiN_x-III) were produced using the method of RF PECVD chamber with three horizontal stainless steel electrodes (Fig. 5.1). N_2 gas was injected with a gas flow rate up to 10 standard cubic centimetres per minute (sccm) through a grounded showerhead electrode (D), which ensured a uniform flow of gas. Due to high nitrogen and silane gas dissociation energy difference, the silane and argon gas mixture SiH_4 (5%) + Ar (95%) entered the field of plasma through a side nozzle in the reactor. The plasma was excited between the shower (D) and the grid (T) electrode using the constant power of a 23 MHz frequency generator (G). The negative (-30V) DC voltage was applied to the sample holder (S). The distance from the electrode T to the shower shape electrode was 3.5 cm (l_1) and 7 cm was the distance (l_2) to the sample holder.

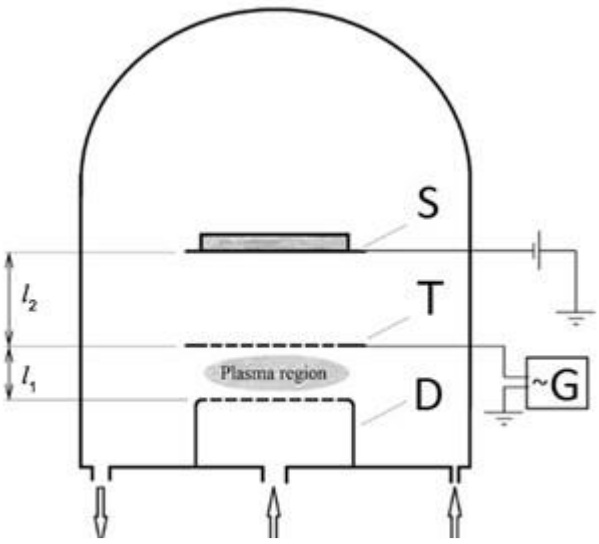

Fig. 5.1 Schematic view of the deposition system. Details are in the text.

The second series of samples (SiN_x-II) were deposited in the CVD chamber without the net electrode T. In this case, the power generator has been connected to the S and D electrodes as in the conventional parallel-plate CVD reactor. The distance between the electrodes was 3.5 cm.

For the deposition of all the layers the temperature of substrate and the pressure of gas mixture in the chamber was 300 °C and 0.2 Torr, respectively.

5.2 FTIR and spectroscopic ellipsometry measurements

The structure of the bonds of SiN_x-III layers was examined using the FTIR method. The FTIR measurements were performed in the specular reflection from the SiN_x samples deposited on aluminium-coated glass substrates, thus, for estimation of density of the bonds double thickness of the layer has been used. As the layer thickness is less than half of the irradiation wavelength, possible changes of the positions of absorption bands may be expected [17].

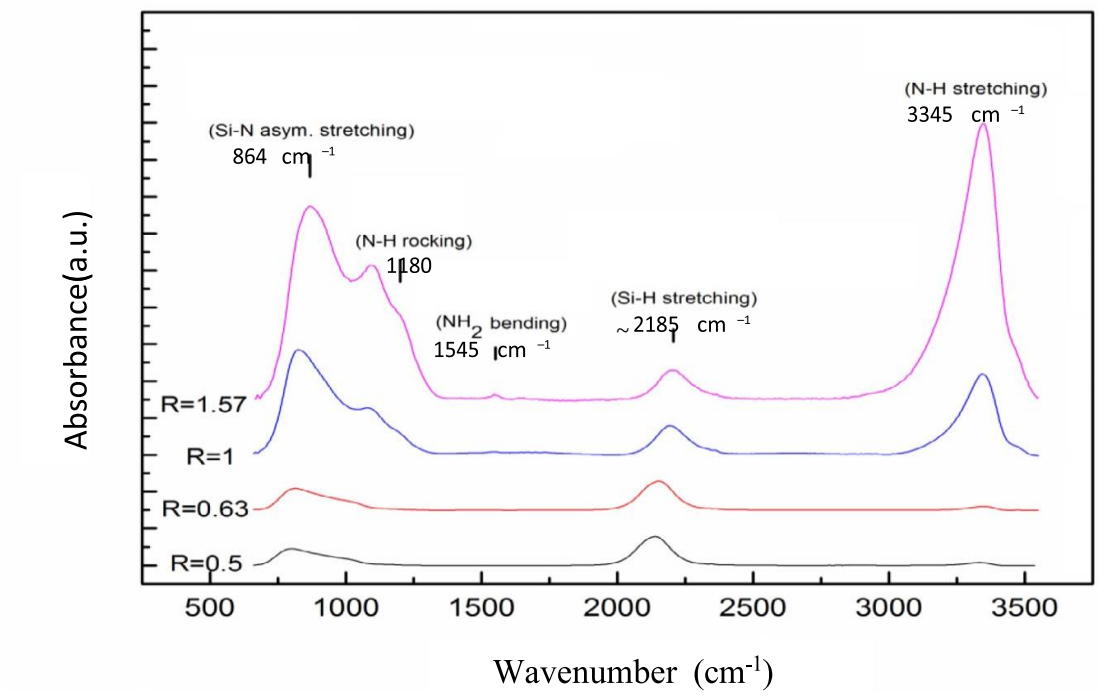

Fig. 5.2 FTIR spectra of SiN_x-III samples grown at different gas ratios.

Figure 5.2 shows the FTIR spectra of the SiN_x-III samples deposited at different gas ratios. Interference effects in the films were removed from the spectra via the base line correction technique, and the spectra were normalized to the ~2185 cm^{-1} absorption band. The peak at ~860 cm^{-1} is assigned to the vibrations of Si–N asymmetric stretching [18]. The shoulder at ~1180 cm^{-1} and the vibration band at ~3345 cm^{-1} are attributed to the N-H rocking and stretching modes, respectively [18, 19]. The peak at ~2185 cm^{-1} is assigned to the Si–H stretching band [18]. This absorption band demonstrates the blue shift with increasing gas ratio. The samples, deposited at higher gas ratios, also exhibit a small peak at 1545 cm^{-1}, which can be assigned to the NH_2 bending vibration [19]. The IR absorption

areas of Si–H and N–H bonds were integrated and multiplied by the constants determined by Lanford et al. [20]. This allowed us to evaluate the density of Si–H and N–H bonds (Table 5.1). The stoichiometry of the film was obtained from the following expression [21]:

$$\frac{1}{x} = \frac{\mathrm{Si}}{N} = 0.084\,\frac{[\mathrm{Si{-}H}]}{[\mathrm{N{-}H}]} + 0.70 \qquad (5.1)$$

Table 5.1. SE and FTIR results of SiN_x-III series of samples.

Dujų santykis (*R*)	**Si-H (10^{22}/cm^3)**	**N-H (10^{22}/cm^3)**	**N/Si (FTIR)**	**n (632 nm)**	**N/Si (SE)**
0,5	1,54	0.19	0.72	2.1	1.0
0,63	1,48	0.33	0.93	2.0	1.1
1	0,38	1.35	1.35	1.9	1.4
1,59	0,12	1.33	1.41	1.6	2.0

An experimental SE data in terms of the ellipsometric parameters Δ and Ψ for the SiN*x*-III sample are presented by dots in Fig. 5.3. The clearly pronounced oscillations are due to interference from the SiN_x layer. The oscillations fade out in the short-wavelength region above the absorption onset of SiN_x. The refractive index of SiN_x was determined from the experimental SE data using the three-phase model: Al covered glass substrate, SiN_x layer with surface roughness, and ambience. The best fit was achieved employing the Tauc-Lorentz model [22]. The obtained refractive index of SiN_x varied in the range from 1.6 to 2.1 (at 632 nm) depending on nitrogen concentration. The insert of Fig. 5.3 shows the refractive index of the SiN_x-III series of samples as a function of wavelength. Silicon rich samples demonstrate higher values of the refractive index. This is a common pattern for silicon nitride. Stoichiometry of the film was estimated from the refractive index *n* according to [23]

$$x = \frac{\mathrm{N}}{\mathrm{Si}} = \frac{4}{3}\,\frac{3.4-n}{3n-0.4}. \qquad (5.2)$$

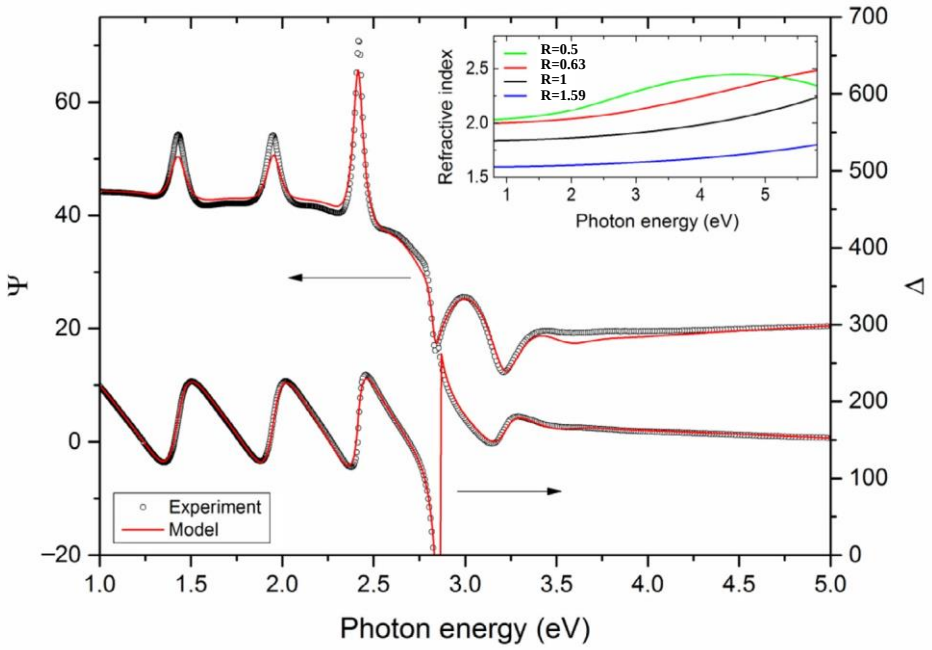

Fig. 5.3 Typical ellipsometric parameters Ψ and Δ for the SiN_x-III film. The fits obtained using the Tauc-Lorentz model are shown as lines. The insert shows the variation of refractive index of the SiN_x-III samples grown at different gas ratios.

The films deposited using the chemical vapour technique contain a significant amount of hydrogen [18, 20], but Eq. (5.2) neglects contribution from hydrogen bonding, resulting only in a rough estimation of stoichiometry. In our research the N/Si ratio, estimated from Eq. (5.2), increases with increasing the gas ratio injected into the deposition system (Table 5.1).

5.3 Surface roughness

Surface roughness of the SiN_x samples, prepared using different configurations of the chamber, was examined using AFM. The stoichiometric layers (x = 1.35 of SiN_x-III and x = 1.21 of SiN_x-II) that have been deposited on aluminium-coated glass substrates were chosen for comparison. Figure 5.4 shows the surface morphology of the films. It is clearly seen that the surface of the SiN_x-II film consists of higher density and larger nanometre-

size grains than ones of the SiN_x-III sample. The measured root-mean-square roughness (R_q) of the area was 9.4 nm and 3.9 nm for the SiN_x-II and SiN_x-III films, respectively. This difference could be due to different configuration of the electrodes in the chamber. In a parallel-plate reactor the surface of the layers is bombarded by the charged particles, which may lead to a rougher surface of the layer. On the other hand, this difference in roughness may also be influenced by different deposition rates because the parallel-plate CVD configuration causes accelerated film growth.

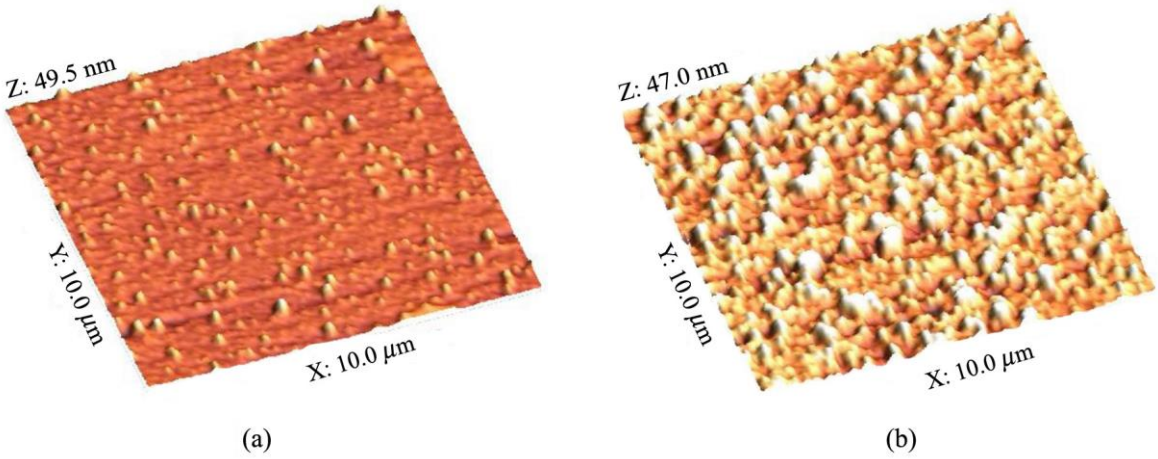

Fig. 5.4. AFM surface images of (a) SiN_x-III (x = 1.35) and (b) SiN_x-II (x = 1.21) samples.

5.3 Optical measurements

The UV–visible absorption spectra of the films deposited on CaF_2 substrates were measured. The optical energy band gap value of the film can be obtained from absorption measurements using the well known Tauc's formula [24]:

$$(\alpha h\nu)^{1/2} = B(h\nu - E_g), \qquad (5.3)$$

where α is the absorption coefficient, B is the constant, $h\nu$ is the photon energy and E_g is an optical band gap. In Fig. 5.5 the Tauc's plots of the deposited SiN_x samples are shown. Linear extrapolation of the curve allows to set E_g because the Tauc's model considers only direct optical transitions. The oscillation observed in the spectrum is determined by the interference fringes in the film. Using a three-electrode CVD chamber it was possible to change the width of the energy gap from 1.85 eV (amorphous silicon) to 5.15 eV (R = 1.59) with increasing the gas ratios R (Table 5.2). The latter electrode configuration was much more sensitive to gas ratio variation than in the case of parallel-plate configuration. Moreover, using the parallel-plate configuration the widest band gap of the samples was only 3.9 eV at R = 10. As expected, the band gap of silicon nitride increased with increasing nitrogen content in the films for both series of the samples.

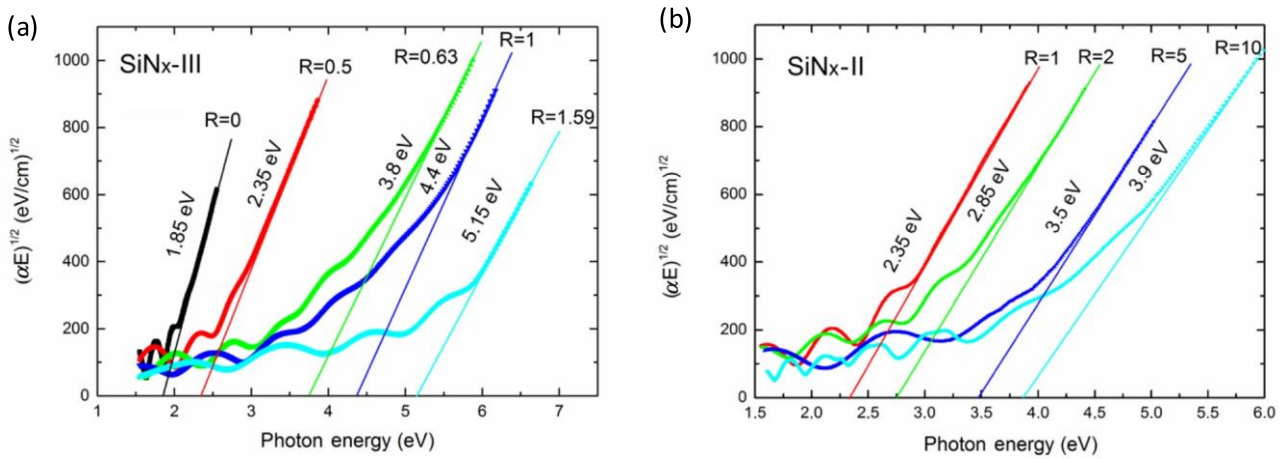

Fig. 5.5. Absorption dependencies (Tauc's plot) of silicon nitride samples deposited in (a) three-electrode and (b) two- electrode CVD chamber.

Table 5.2. Deposition parameters and properties of SiN_xlayers.

Series of sample	Deposition rate, nm/min	N_2, sc cm	SiH_4+Ar, sc cm	Ratio R	E_g, eV	Thickness, nm	N/Si (EDS)
III	10.1	0	6.3	0	1.85	606	–
III	4.63	6.3	12.6	0.5	2.32	556	0.69
III	4.86	6.3	10	0.63	3.8	585	0.98
III	4.95	6.3	6.3	1	4.4	594	1.35
III	4.85	10	6.3	1.59	5.15	582	1.44
II	8.14	6.3	6.3	1	2.35	570	0.62
II	8.35	12.6	6.3	2	2.85	585	0.76
II	8.12	31.5	6.3	5	3.5	569	1.01
II	8.28	63	6.3	10	3.9	580	1.21

5.4 Breakdown strength and leakage current

For application purposes a critical parameter of the dielectric layer is a magnitude of breakdown electrical field. Although the breakdown voltage is an intrinsic property of the material, however, the maximal breakdown magnitude may vary depending on the surface roughness, imperfections as well as on the thickness of the film. Even the area of the electrode may have an influence on the magnitude of breakdown voltage.

The samples, which have been tested using AFM, were chosen for electrical measurements (Fig. 5.6). The measurements of current–voltage (*I–V*) characteristics were made for the both polarities of voltage on the electrodes, however, the *I–V* dependences were identical.

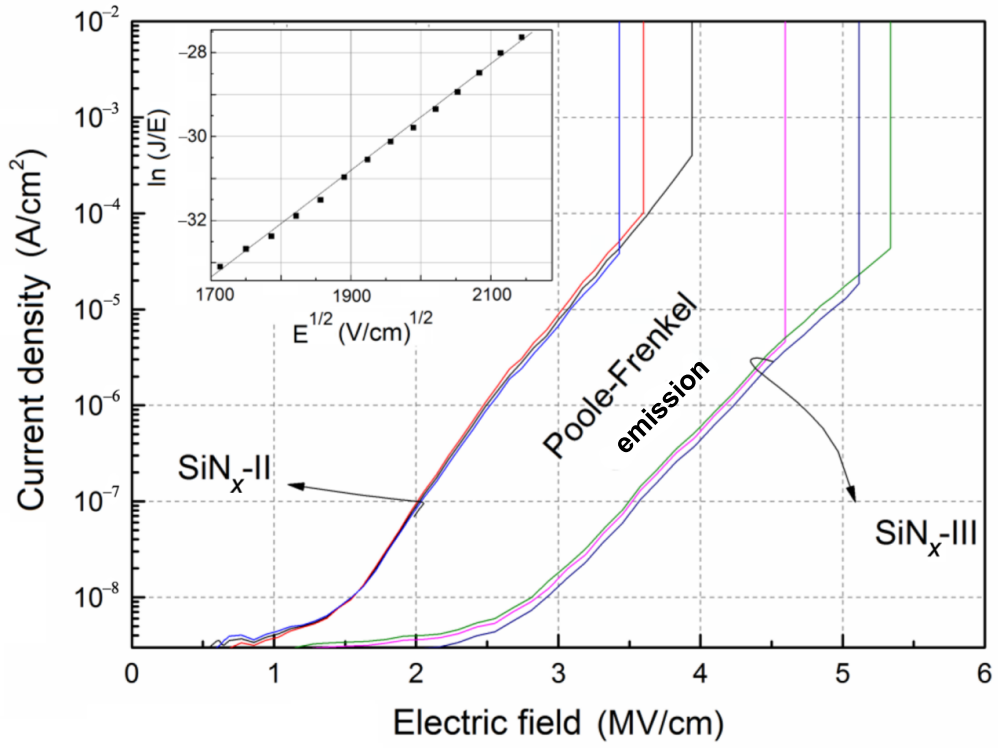

Fig. 5.6. Dependences of current density on electric field of SiN_x-II (x = 1.21) and SiN_x-III (x = 1.35) samples. The insert shows a typical linear part of PF plot.

The current density dependence at high electrical field can be interpreted as the Poole-Frenkel (PF) emission [25]. The PF emission occurs due to the field-enhanced thermal

emission of trapped electrons to the conduction band, and the current density is described by a general expression

$$J = AEexp\left[-\frac{q\phi_B - \beta\sqrt{E}}{\xi kT}\right], \qquad (5.4)$$

where $\beta = q/\pi\varepsilon\varepsilon_0$, A is the constant, Φ_B is the barrier height, ε is the dielectric permittivity, k is the Boltzman constant, and ξ is the correction factor which may vary between one and two, depending on the amount of the compensating acceptor. The PF plot of ln(J/E) versus E yields a straight line:

$$\ln\left(\frac{J}{E}\right) = \frac{\beta\sqrt{E}}{\xi kT} + \left(\ln A - \frac{q\Phi_B}{\xi kT}\right). \qquad (5.5)$$

The typical linear part of the PF plot is shown as an insert in Fig. 5.6 and is taken as the evidence of PF conduction. The slope of the PF plot is proportional to β and can be expressed by

$$S = \frac{\beta}{\xi kT}. \qquad (5.6)$$

The experimentally measured slopes for the SiN_x-II and SiN_x-III samples are 0.0129 and 0.0121, respectively. The theoretical value of the slope S for stoichiometric Si_3N_4 (ε = 7) is 0.0111, which is fairly close to the measured values. If we assume that ξ = 1, then ε = 5.2 and 5.9 for the SiN_x-II and SiN_x-III samples, respectively. The discrepancy may occur since ξ is not strictly equal to one and depends on the nature and density of traps in the film. For the determination of ε we consider that electrical field in the film is homogeneous, however, it is known that the charge carriers injected into the SiN_x film are trapped and create a space charge. The dielectric constant in the visible range (~500 nm) is ~4 and the static dielectric constant is around 7, therefore, the dynamic dielectric constant must range between 4 and 7 [13].

The SiN_x samples deposited using the three-electrode CVD reactor, at the same electric field, demonstrated lower current density compared to that of the samples prepared using the two-electrode configuration CVD reactor. Since most of field-effect devices operate at approximately 2 MV/cm electrical field, it is reasonable to compare current density particularly at this electrical field strength. At 2 MV/cm, the average current density is 3.6

$\times 10^{-9}$ A/cm^2 and 7.9×10^{-8} A/cm^2 for the SiN_x-III and the SiN_x-II films, respectively. The measurements on different electrodes of the same sample did not show any significant fluctuation of current magnitude while the breakdown strength ranges from 4.6 MV/cm to 5.3 MV/cm for the SiN_x-III and from 3.4 MV/cm to 3.9 MV/cm for the SiN_x-II films. In our case, taking into account the AFM measurements, lower breakdown strength of the SiN_x-II film can be explained by higher surface roughness and not necessarily by the intrinsic properties of the material. In the region of weak electrical fields the current density dependence on the electric field corresponds to the Ohm's law. In a weak electric field (0.5 MV/cm), the average estimated resistance of the SiN_x-III and SiN_x-II films are 5.47×10^{14} Ω cm and 2.4×10^{14} Ω cm, respectively. Although the electrical properties of PE CVD silicon nitride depends on the method of deposition, the both samples demonstrate a decent resistivity value of $>10^{13}$ Ω cm [27].

In conclusion, it was found that SiN_x layers deposited in three electrode PECVD reactor showed better electrical, optical and morphological properties. These features are required for the formation of electroluminescent SiN_x/a-Si:H SLs.

6. SIN_X/A-SI:H SUPERLATTICE STRUCTURES [S2]

6.1 Experimental details

The multilayers with 7.5 a-Si:H/SiN_x periods of sublayers have been deposited on the ITO coated glass substrates using three electrode PECVD chamber. The plasma excitation frequency of 13.5 MHz has been used and the temperature of substrate during deposition has been fixed at 300 °C. The silicon layers have been deposited using gas mixture of 5% silane and 95% argon at total gas flow of 6.3 sccm and 27 Pa pressure. For deposition of silicon nitride layers the nitrogen has been injected (6.3 sccm) into the plasma enhanced chemical vapour deposition chamber, additionally. For the UV-visible light absorption measurements, the individual SiN_x and a-Si:H layers have been deposited on CaF_2 crystals. An E_g of the films has been estimated using Tauc's method [24]. The band gap of deposited SiN_x and a-Si:H films was 5.1 eV and 1.7 eV, respectively.

The schematic structure of the samples is shown in Fig. 6.1. The first series of a-Si:H/SiN_x samples have been deposited by varying the thickness of the SiN_x sublayers from 2 nm to 5 nm while the thicknesses of a-Si:H layers have been fixed at 3.5 nm. The second series of samples have been deposited of fixed thickness (2 nm) of SiN_x sublayers while the thickness of a-Si:H sublayers has been varied from 1.5 nm to 3.5 nm. The samples have been investigated using FEI TECNAI F20 electron transmission microscope (TEM) equipped with a field emission electron gun. Accelarating voltage was 200 kV and bright field images were recorded on GATAN Orius CCD camera. The thickness of layers has been determined from the deposition rates and these results were confirmed by TEM measurements. The aluminum electrodes of 2 mm diameter have been deposited on top of the layers as cathode. The samples have not been post annealed.

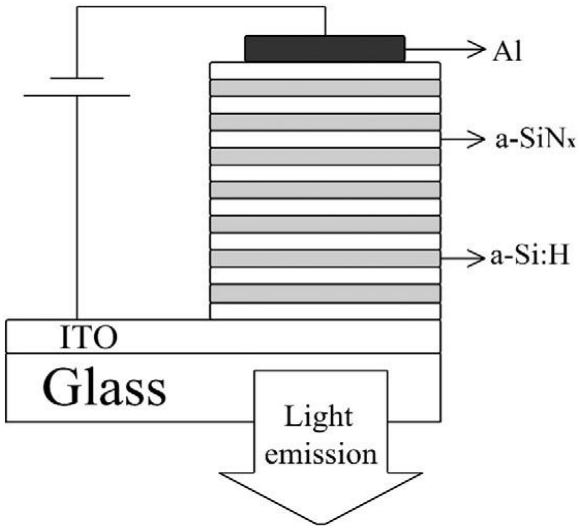

Fig. 6.1. Schematic view of the Si/SiN_x device structure

6.2 Structural properties of SiNx/a-Si:H SLs

Cross-section of transmission electron spectroscopy (TEM) micrograph of a-Si:H/SiN_x SLs is shown in Fig. 6.2. An individual SiN_x and a-Si: H layers of the sample are visible in the TEM image as dark and bright stripes. As can be seen from the image the deposited structure replicates the roughness of the ITO substrate. The insert of Fig. 6.2 shows a silicon nanoparticle embedded between two SiN_x sublayers. In a high resolution TEM image we can observe a crystalline structure of Si nanoparticle.

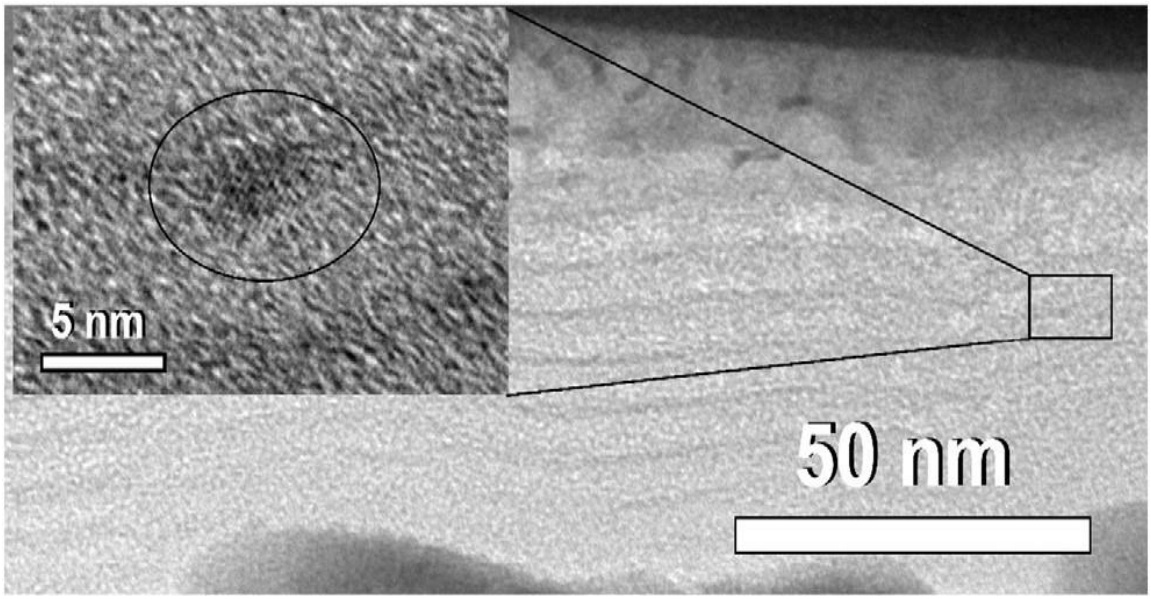

Fig. 6.2. TEM image of a-Si:H/SiN_x SLs. The insert shows a formed silicon nanocrystallite in the interface of two SiN_x layers

6.3 Electrical properties

J–V characteristics of the first series of samples of different thickness of SiN_x barrier layers are shown in Fig. 6.3. The thicker samples demonstrates higher onset voltage of EL while the shape of the spectrum remains almost unchanged. Measurements under reverse bias showed similar J–V characteristics with slightly lower current densities. The dominant current mechanism is considered to be Fowler–Nordheim (FN) tunnelling under high electric field. This can be verified by fitting J–V characteristics in a FN plot (insert of Fig. 6.3). Since the electrical resistivity of SiN_x is at least few orders of magnitude

higher than the resistivity of a-Si:H, for numerical modelling it was assumed that the electric field mainly is concentrated in SiN_x sublayers [18].

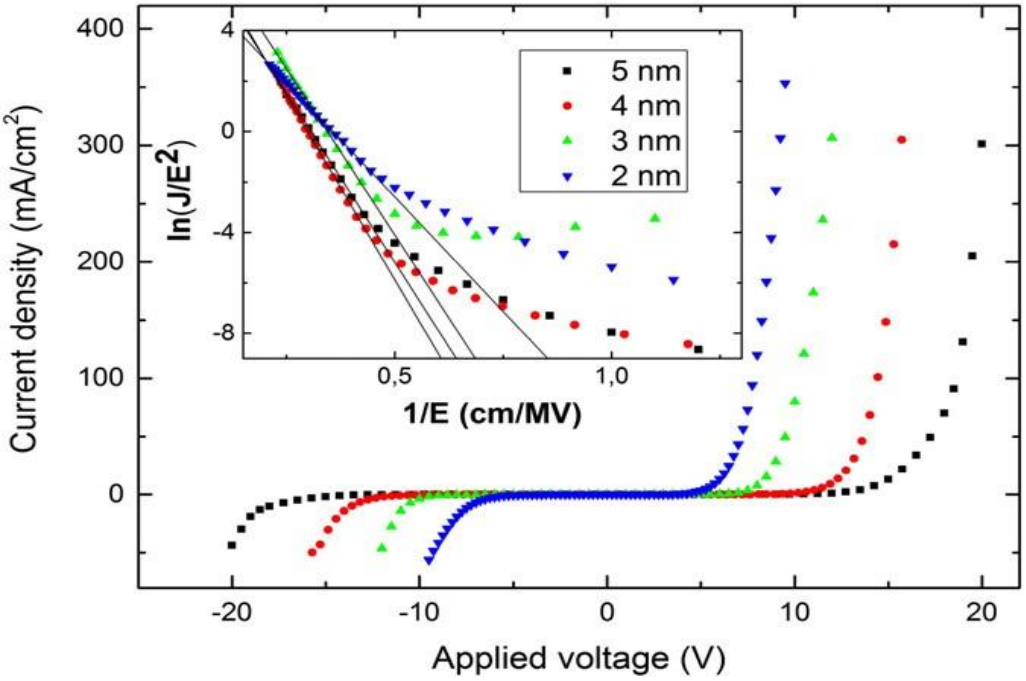

Fig. 6.3. J–V characteristics of Si/SiN_x SLs with different thicknesses of SiN_x sublayers. Insert shows plotted ln(J/E^2) as a function of E^{-1}.

SLs deposited on c-Si wafer usually suffers from hole overflow into the active region due to the lower barrier height for holes compared to the barrier height for electron injection from transparent conducting layer (ITO or aluminium doped zinc oxide) [27, 28]. Fig. 6.4 shows the proposed energy level diagram of our device [29–31]. Although, the barrier for holes is decreased by 0.6 eV compared to the barrier for electrons inside the active region the injection of electrons from Al electrode should exceed the injection of holes from ITO due to the relatively lower barrier by 0.4 eV.

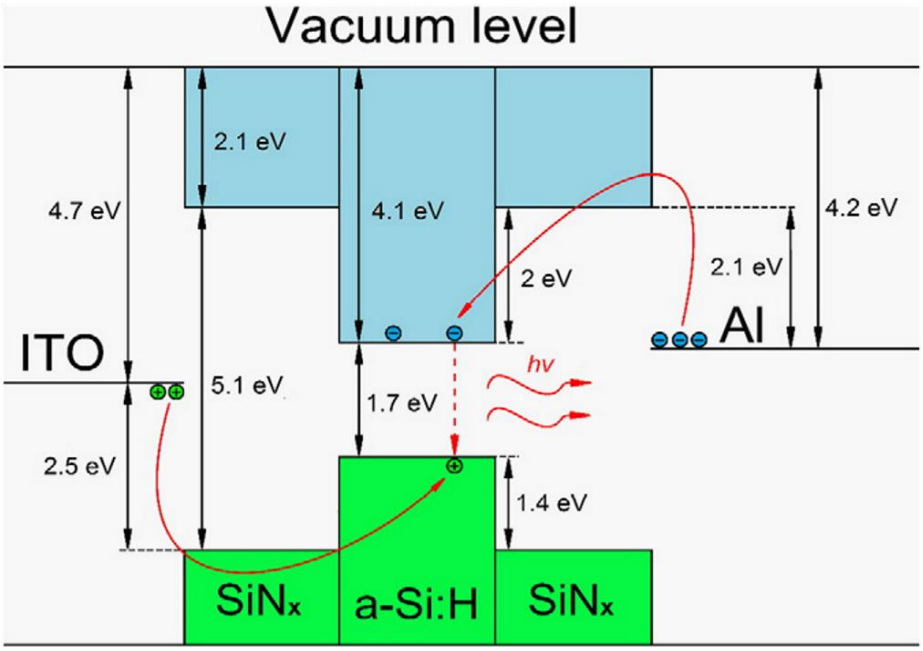

Fig. 6.4. A schematic energy level diagram of the device.

6.4 Electroluminescence from SiNx/a-Si:H SLs.

Fig. 6.5 shows the EL spectrum of the first series of sample with 2 nm thick SiN_x sublayers measured under forward bias of 11, 12, 13 and 14 V. The fitting performed on the spectrum yields two Gaussian peaks at 560 nm and 700 nm. The position of both peaks is independent on applied voltage. The total integrated EL intensity (L_Σ) increases linearly with increasing the current density (insert of Fig. 6.5). This linear behaviour suggests the bipolar injection of charge carriers into the active region with following emissive recombination and points to the absence of impact ionization mechanism. In the case of impact ionization the energy of injected carrier depends on the applied voltage and this would lead to super-linear dependency of integrated EL intensity vs. current density [11]. It must be noticed that integrated EL intensity of 700 nm peak grows faster compared to the integrated intensity of 560 nm peak (insert of Fig. 6.5).

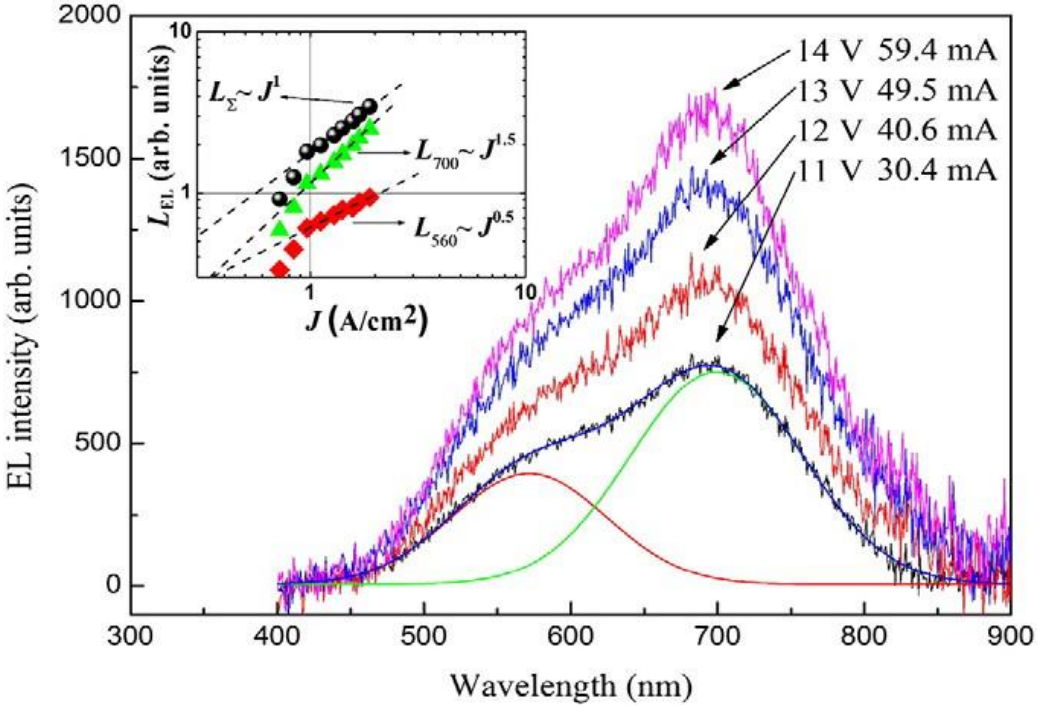

Fig. 6.5. The EL spectra of a-Si/SiN_x SLs with SiN_x sublayers thickness of 2 nm under forward bias. Decomposed bands: 700 nm and 560 nm. The insert shows linear relation between integrated EL intensity L_Σ and the current density.

There are a lot of possible origins of the electroluminescence in a-Si: H/SiN_x SLs. The EL may be caused by quantum confinement effect in the structure, or by luminescence from localized states in the a-Si:H and SiN_x interface, or by localized states inside the bulk of SiN_x sublayers [10]. Also the emission in near-IR band could be related to the light emission from Si nanoparticles embedded in the silicon nitride matrix [32].

After an annealing the Si-rich materials the excess of silicon forms Si quantum dots (Si-QDs) and this leads to enhancement of EL. Although our SLs have been formed without post annealing, we observed a few Si-QDs in TEM micrographs, one of which is shown in insert of Fig. 6.2. As follows from TEM micrograph the size of shown nanocrystallite is approximately 4 nm. The search of slices demonstrated that the observed nanocrystallites of a similar size are mainly in a-Si:H sublayers. However, the well-defined nanocrystallites of smaller dimensions were not observed neither in a-Si:H, nor in SiN_x. We make an assumption that crystallization centres in our SLs occur at the interface of a-Si:H/SiN_x and this leads to rapid growth of Si QD during the deposition. We cannot

eliminate possibility that QD of smaller than 4 nm may be formed in the interface or in SiN_x close to a-Si:H/SiN_x interface and, therefore, the possible EL from the surfaces of Si nanocrystals cannot be excluded. However, in TEM micrographs the smaller than 1.5 nm nanocrystallites have been not observed.

According to Ref. [33] the quantum confinement effect in nanocrystallites larger than 1.5 nm size may not be sufficient to overcome the indirect gap of c-Si, thus, may not cause the EL.

According Ref. [34, 35] the origin of peak in the vicinity of 700 nm could be caused by recombination of injected charge carriers trapped in the localized states of SiN_x sublayers. However, with reducing the thickness of a-Si:H layers the 700 nm peak shifts to higher energy (Fig. 6.6) although this should not be seen if the origin of this peak is attributed to the defects into SiN_x layers. As can be seen from energy diagram shown in Fig. 6.4, the EL peak at 700 nm corresponds to the width of band gap of the a-Si:H sublayer. Also as follows from Fig. 6.6, this EL band blue-shifts from 700 nm to 650 nm with decreasing the thickness of aSi:H sublayers from 3.5 nm to 1.5 nm (the thickness of SiN_x barriers was 2 nm). With reducing the thickness of the a-Si:H sublayer the emission shifts to higher energy region due to the quantum confinement effect. Widening of the optical band gap (E_g) of a-Si:H layer due to the quantum confinement effect could be estimated using the Kronig–Penny model for a free electron in a one-dimensional square-wave periodic potential [36]. For modelling we assumed the parameters as follows: optical band gap 1.7 eV of a bulk a-Si:H; 2 nm thickness of SiN_x; valence and conduction band discontinuities at the a-Si:H/SiN_x interface $_c$ = 2 eV and $_v$ = 1.4 eV, respectively. The insert of Fig. 6.6 shows a good agreement between experimentally measured shift of 700 nm peak position and the calculated E_g values (solid line) as a function of a-Si:H layers thickness. This suggest that the origin of EL at 700 nm is due to the radiative recombination within a-Si:H layers embedded into SiN_x matrix and is not related to EL from SiN_x defects.

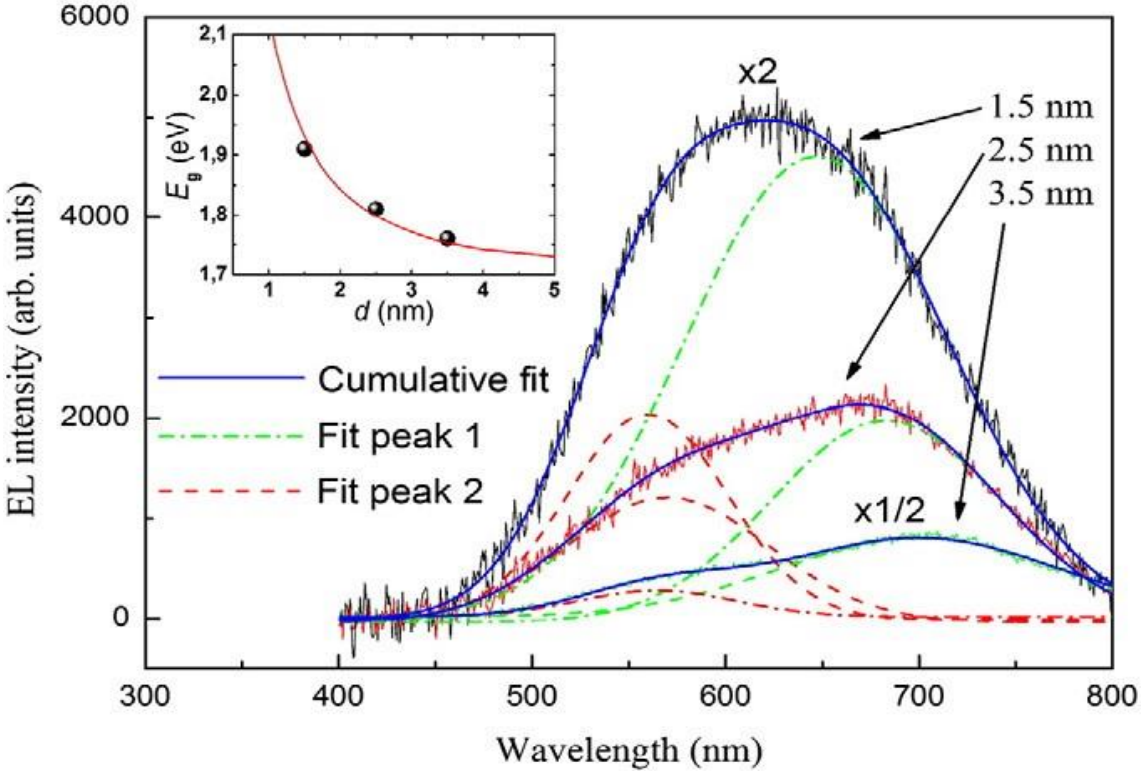

Fig. 6.6. EL spectra of a-Si:H/SiN_x SLs with different thicknesses of a-Si:H sublayers at 14 V. The insert shows optical band gap E_g dependence on the thickness of a-Si:H sublayers (the solid line is calculated values).

The EL peak at 560 nm, on the other hand, does not shift with decreasing the thickness of a-Si:H. Also the relative intensity of peak at 560 nm is unchanged with decreasing the thickness of SiN_x which excludes the assignment of it to EL from defect centres in SiN_x layer, therefore, the high energy band may be attributed to radiative recombination from defect states or smaller than 1.5 nm nanocrystallites at a-Si:H/SiN_x interface [7]. This is supported by EL dependencies on density of current (insert of Fig. 6.5) of integral EL of peak at 560 nm (L_{560}), 700 nm (L_{700}) and of integral of the whole EL signal (L_Σ). The $L_{700} \sim J^{1.5}$ and $L_{560} \sim J^{0.5}$, while integral EL demonstrates linear dependence on J. The latter dependencies may be explained by redistribution of charge carriers between interface states and a-Si:H sublayer, which is induced by increasing electric field. The increasing electric field empties interface states, thus, reduces EL at 560 nm, while the released charge carriers get to a-Si:H sublayer and increase EL at 700 nm, correspondingly.

In conclusion, we have fabricated luminescent a-Si:H/SiN_x superlattice structures (SLs) with different thicknesses of both a-Si:H and SiN_x sublayers. The TEM micrograph revealed the small amount of silicon nanocrystalls. The main EL peak at ~700 nm is related to radiative recombination in thin a-Si:H layers and the peak at higher energy (~560 nm) is originated from a-Si:H/SiN_x interface defect states.

7. Ce:SiN_x ELECTROLUMINESCENT LAYERS [S3]

7.1 Experimental details

A seven light emitting devices have been formed on the indium tin oxide (ITO) coated glass. The schematic view of the sample is shown in Fig. 7.1. The thin layer of SiN_x (~27 nm) has been deposited on top of ITO layer using three electrode PECVD chamber. The temperature of substrate heater inside the PECVD chamber was set to 300 °C. The nitrogen gas has been used as N precursor at the gas flow rate of 5 standard cubic centimetres per minute (sccm). The gas flow of the 5% silane and 95% argon gas mixture has been set to 6.3 sccm with a total gas pressure of 30 Pa in the PECVD chamber. The plasma excitation frequency has been set at 13.5 MHz. Subsequently a thin layer of cerium has been sputtered from 99.9% purity cerium target via direct current sputtering method.

The sputtering has been carried out under an argon gas flow of 6.3 sccm at 13 Pa pressure with an applied voltage of 4.6 kV. An each sample has been subjected to the sputtering treatment for the different period of time: 25 s, 50 s, 75 s, 100 s, 200 s and 500 s. After deposition of cerium, the ~27 nm of SiN_x layer has been deposited on top, as discussed above. Also the reference device have been prepared without cerium doping but in accordance with the same preparation procedure.

The bulk SiN_x layer have been deposited on the CaF_2 crystal for light absorption measurements. The absorption spectrum was collected in the VU/Vis/Nir spectral range

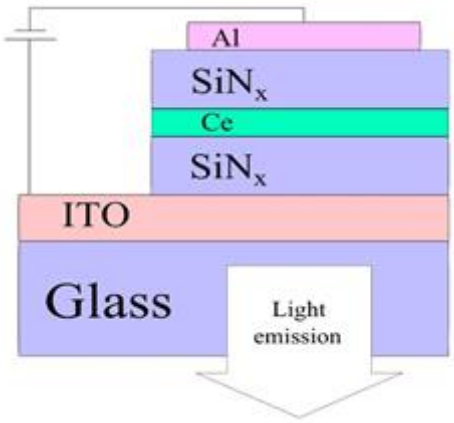

Fi

The band gap of 4.7 eV of the films has been estimated using Tauc's method [24]. A SiN_x layer demonstrated penetration depth δ_p = 63 nm for 258 nm wavelength radiation.

Based on the results of the absorption measurements the Yb:KGW laser has been selected for lattice annealing purpose. The wavelength of femtosecond (τ = 280 fs) “PHAROS” laser (fundamental wavelength λ = 1030 nm) has been converted into 258 nm using nonlinear crystals. The fundamental laser power has been locked by internal laser source power lock and the repetition rate of laser

pulses was set to 200 kHz. An experiment has been performed using “Aerotech” linear translation stages and positioning sample regarding laser beam. The controllable density of light pulses was set to 2000 pulses per millimetre of length in both directions of X and Y axis. The diameter of laser beam at $1/e^2$ was 2.8 mm and the plano-convex focusing lens of fused silica with F = 150 mm has been used. An average energy of single pulse has been set to 0.26 μJ to process the samples and λ/4 wave plate has been used to produce circular polarization of light. With the purpose to avoid surface oxidation during laser processing, samples have been placed in the inert Argon gas environment. The rectangular shaped aluminium electrodes of 2 mm^2 area have been vacuum deposited on top of the laser treated and untreated parts of the surface. The laser treatment experiments have been performed in “Altechna R&D” laboratory.

7.2 Structural properties of Ce:SiN_x layers

In Fig. 7.2 the cross-section of as deposited sample obtained using a transmission electron spectroscopy micrograph and the linear profile of energy- dispersive X-ray (EDX) spectrum are shown in Fig. 7.3a. The scan of EDX line profile confirms the compositions of the layers and the TEM image clearly indicates buried cerium layer in the SiN_x lattice The sputtering from cerium target for a 500 s results the deposition of ~12 nm thick cerium layer, which corresponds to the deposition rate of ~0.24 Å/s. In the investigated samples the thicknesses of cerium layers were calculated according to the deposition rate and corresponds to 0.6 nm, 1.2 nm, 1.8 nm, 2.4 nm, 4.8 nm, 12 nm thicknesses and the samples were named N_0, $N_{0.6}$, $N_{1.2}$, $N_{1.8}$, $N_{2.4}$, $N_{4.8}$ and N_{12}, respectively, where index is referred to thickness of the cerium layer. In Fig. 7.3b the EDX profile scan of N_{12} sample after the laser treatment is shown. It is seen that the cerium distribution profile

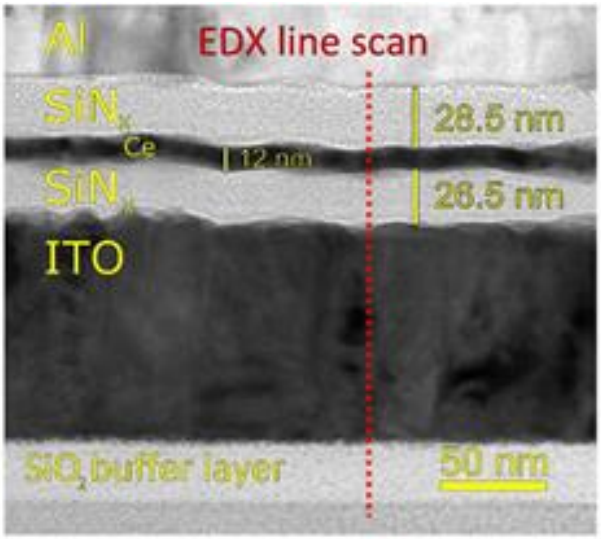

Fig. 7.2. TEM cross-section image

spreads into the SiN_x layer and, after the laser annealing, a full width at half of concentration maximum increases from 16.7 nm to 24.4 nm. It must be noted that the real distribution may vary due to the oxidation of lamella and the roughness of layers junction.

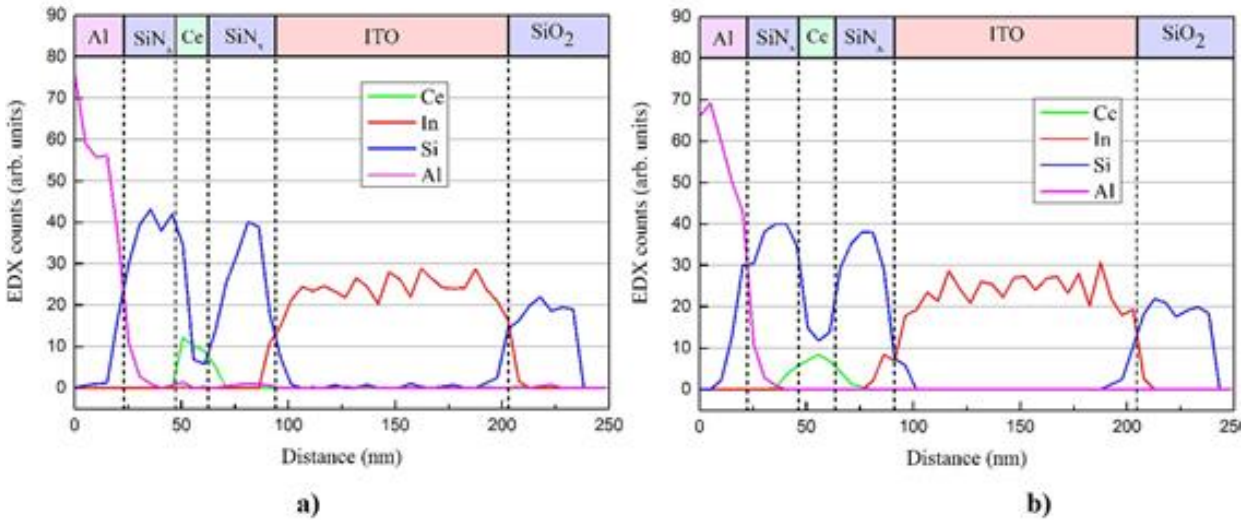

Fig. 7.3 a) EDX line profile of the N_{12} structure before and b) after laser treatment.

7.3 Electrical properties

In Fig. 7.4 the J-V characteristic of laser annealed $N_{1.2}$ sample is shown, as example. The J-V dependences have been measured under the reverse polarities of voltage showed the same pattern with a lower current densities due to different band offset of the aluminium and ITO [29, 31]. It is worth to emphasize, that the external quantum efficiency of our device is close to 10^{-6} order of magnitude, therefore, the EL measurements under reverse polarity demonstrates only a trace of electroluminescence and will not be discussed. The Poole-Prenkel (PF) thermionic emission [25] is usually applied for description of the conduction mechanism in such dielectric and amorphous materials as SiN_x. Also, Fowler-Nordheim tunnelling model can be used when the conduction through the defects or impurities is expected. In our case, due to that plot of ln(J/E) versus $\sqrt{E}$ yields a straight line, in the region of a high electric field the current density dependences are well fitted using PF conduction model (the insert of Fig. 7.4). It was assumed that the voltage drops only in an insulating SiN_x layer. However, nevertheless the samples with a thicker layer of cerium showed a higher conductivity the thickness of SiN_x

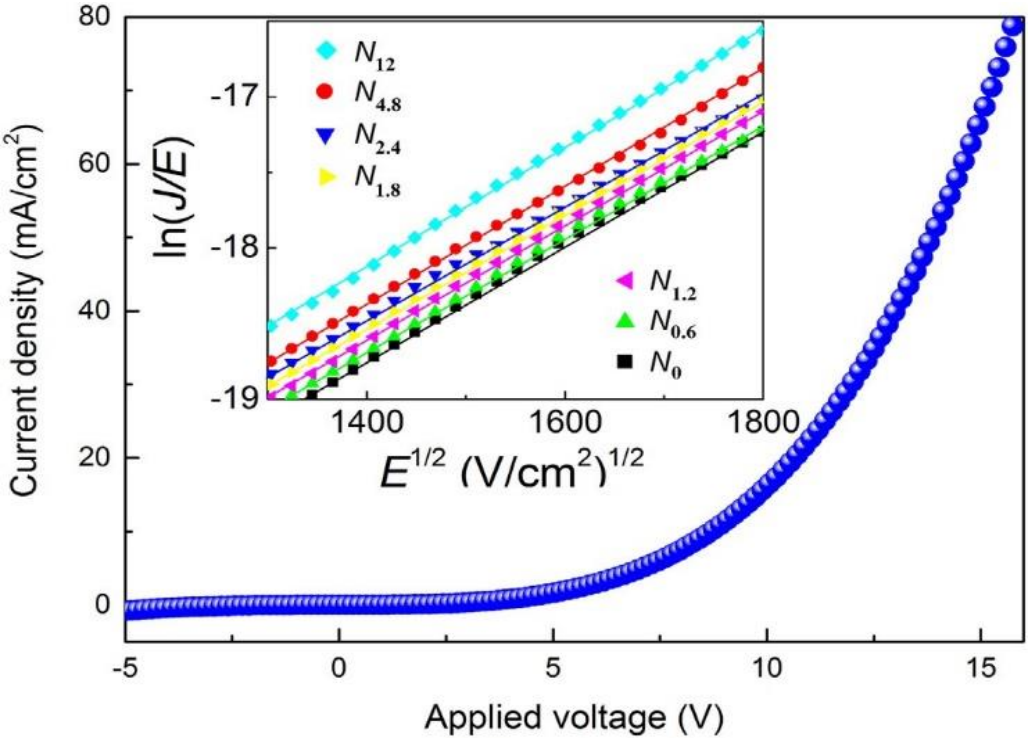

Fig. 7.4. The V-J characteristic of $N_{1.2}$ sample. The insert shows ln(J/E) plotted as a function of $E^{1/2}$.

for all samples were the same. Such a pattern could be explained by the diffusion of the cerium into SiN_x lattice during the laser annealing. This assumption was verified by the measurement of J-V dependences of the laser untreated parts of the samples. The unprocessed samples demonstrated a lower conductivity which almost did not depend on the thickness of cerium, therefore, the SiN_x/Ce/SiN_x structure could be interpreted as a sum of three resistors connected in series. After laser treatment the cerium diffuses into the SiN_x layers and creates a more conductive paths for the injected charge carriers.

7.4 Electroluminescence from Ce:SiNx layers

The turn on voltage of LEDs varied from 7 V to 10 V with a current density at around of 5 mA/cm^2 depending on the conductivity of the structure. An evolution of EL emission spectra of the $N_{1.2}$ sample on current density is shown in Fig. 7.5. The SiN_x LEDs with and without cerium doping emit a broad band in the range from 500 nm to 800 nm wavelength. The attribution of this peak is followed by a lot of debates. Usually the origin

of this band is assigned to EL from silicon quantum dots (Si-QD) embedded in the silicon nitride matrix [32] or from the SiN_x defect states [37]. According to the work of Brown and Rand [38], Si-Si bonds form a σ and σ* states near the valence and conduction bands respectively while silicon dangling bond (K^0) forms a gap state in about the midgap. The silicon dangling bond is a dominant trap and recombination centre in silicon nitride, which may be radiative or non-radiative. The energy distribution of localized states is responsible for broadening of a spectra. The centre of EL band should arise in the wavelength close to the half of the energy of SiN_x band gap, thus, emission at 650 nm is reasonable to expect. Moreover, this band does not change its position dependently on the magnitude of injected current. According to Ref. [39] this behaviour suggests the origin of EL from defect states rather than EL due to the contribution of small-sized Si nanoparticles. Also, the analysis of TEM micrographs of our samples did not reveal any signs of formation of silicon quantum dots in the films.

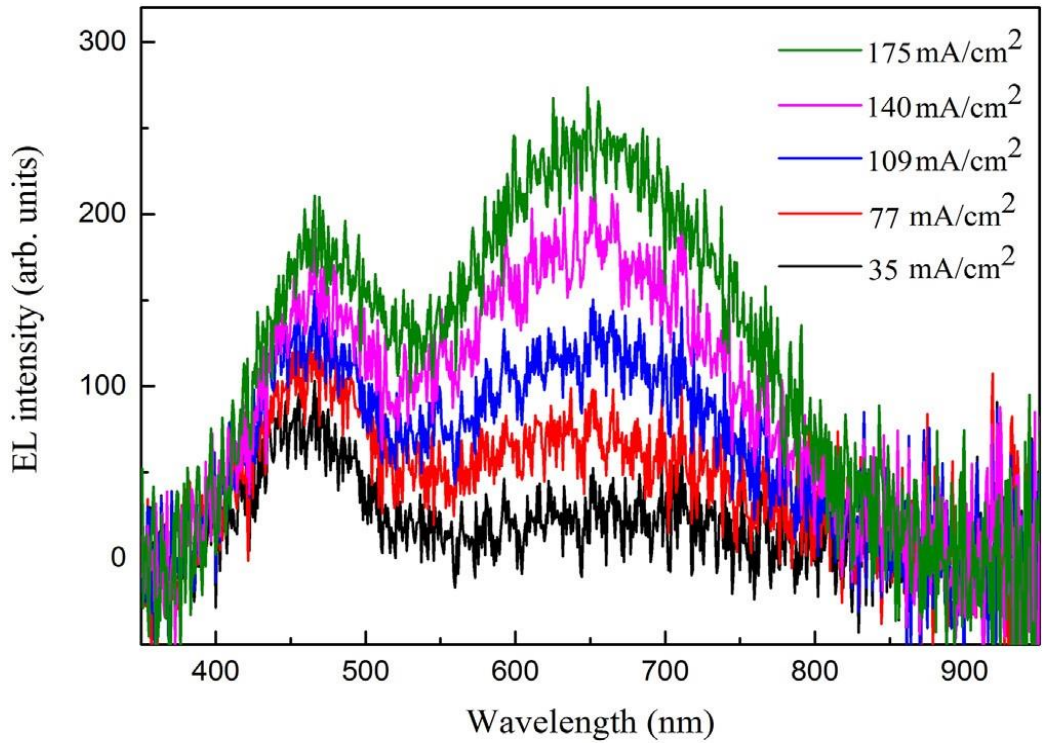

Fig. 7.5. The EL spectra of $N_{1.2}$ sample under forward bias.

The Cerium doped samples exhibited a wide peak at 460 nm wavelength (Fig. 7.6), which could be assigned to radiative transition from 5d-4f energy levels. Though, the position of 460 nm peak shifts slightly to the red wavelength with increasing of applied voltage, however, fitting of the spectra by two Gaussian peaks showed no trend in shifting of position whatsoever. On the other hand, the intensity of 460 nm peak strongly depends on the concentration of the cerium in the structure. The evolution of 460 nm peak is shown by dashed lines in Fig. 7.6. The EL spectra were taken at fixed current density of J=140 mA/cm^2. With increasing of Ce layer thickness in the film, at low Ce thicknesses the 460 nm peak intensity strengthens, achieves maximum and, afterwards, starts to quench the EL emission until it disappears at all. The dependency of integral EL intensity of 460 nm band on the thickness of deposited cerium is shown in the insert of Fig. 7.6. If we assume that cerium atoms are uniformly distributed in all the samples then the cerium concentration would vary in the range between 10^{19} cm^{-3} and 10^{20} cm^{-3}, which is the upper limit for the solubility of RE ions in the Si-based materials [40]. Also the EDX line scan suggests that distribution is similar to Gauss rather than

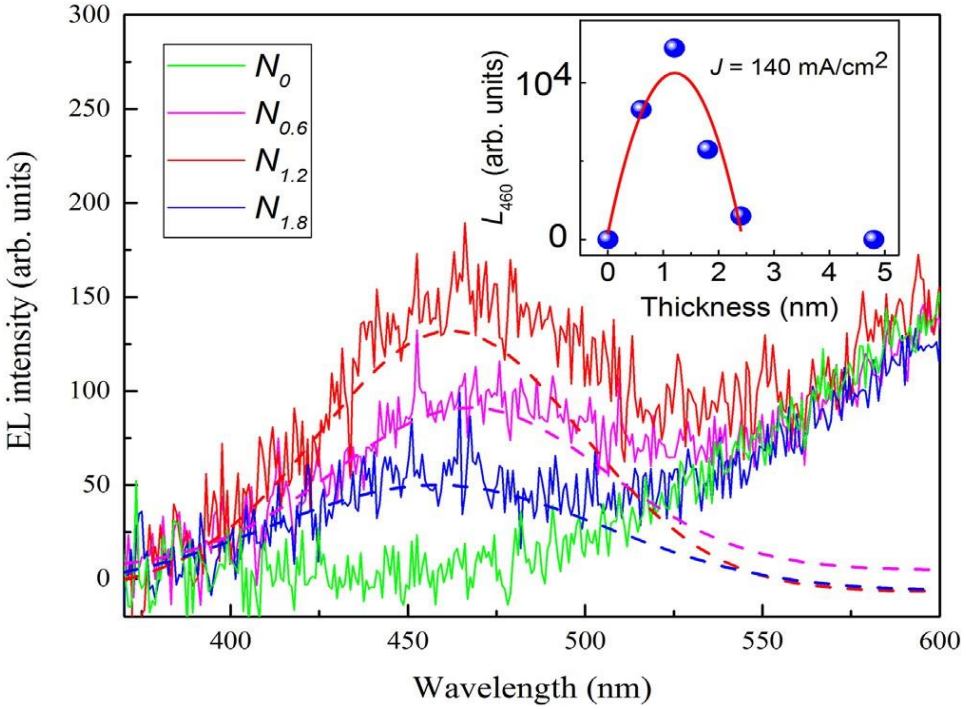

Fig. 7.6. Evolution of 460 nm peak intensity for different samples at fixed J = 140 mA/cm^2 density of current. Dashed lines shows the decomposed 460 nm band. In insert the dependence of EL integral intensity of 460 nm band on cerium thickness is shown.

homogeneous, therefore, the formation of optically inactive cerium clusters are very likely [41]. The 5d–4f transitions are partially allowed due to the odd crystal field component, when Ce ions are incorporated into the host matrix. However, the concentration quenching effect takes place when at high concentrations the Ce^{3+} centres start to interact with each other and disrupts the local periodic field [42]. The 460 nm band was not observed in the laser untreated samples, therefore we speculate, that after laser treatment, the thin layer of cerium is tending to diffuse into host lattice and form a Ce^{3+} bonds while the thicker layers of cerium remains in non-radiative form. Also, the dependency of integral EL intensity of each band on current density is shown in Fig. 7.7. With increasing the density of current the integrated intensity of 650 nm peak (L_{650}) raises more rapidly than intensity of 460 nm band (L_{460}). Although, the integral of total EL signal follows the linear dependence on J, the intensities of two distinguished bands corresponds to $L_{460} \sim J^{0.6}$ and $L_{650} \sim J^{1.4}$. This strongly indicates that the origin of these emission bands are different.

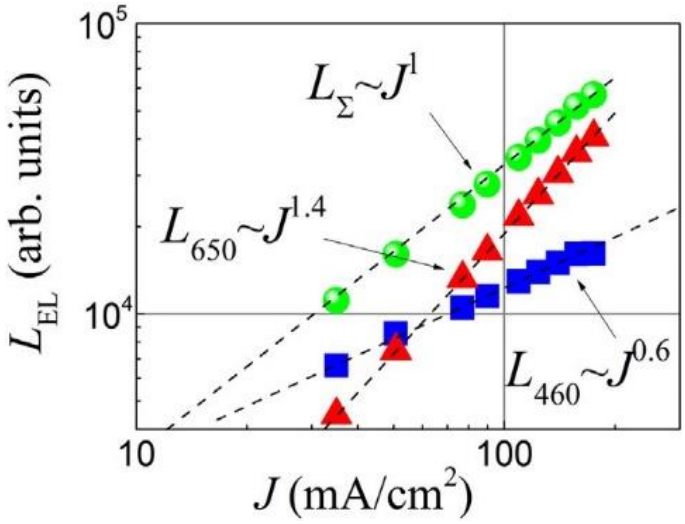

Fig. 7.7. The dependencies of integral EL intensity and of different bands on density of current

The dominant recombination mechanism of our device can be determined using Z-parameter analysis [43]. If we neglect the leakage current, the net recombination from the injected current can be estimated from the following expression:

$$I = qV_aR(n), \quad R(n) = An + Bn^2 + Cn^3, \qquad (7.1)$$

Here I is a total current, N is a charge carrier concentration and V_a is an active volume. A, B and C are coefficients associated with non-radiative, bimolecular and Auger recombination processes, respectively. The output power of EL (P) is related with radiative current (I_r) as:

$$P \propto I_s \propto n^2. \qquad (7.2)$$

Therefore, Eq. (7.1) can be converted to a following expression [28]:

$$\ln(I) = Z \ln(P^{1/2}) + C \qquad (7.3)$$

In Eq. (7.3) the Z parameter may vary in the range from 1 to 3. The Z parameter can be evaluated from experimental data by fitting the linear part of $\ln(P^{1/2})$ versus ln(I) dependency. In our devices the Z value varies in the range of 1.4 to 1.9 (Fig. 7.8). The lowest Z value (1.4) was estimated in the sample with 4.8 nm of cerium. This suggests that, in this case, there is no single dominant recombination mechanism in the structure but rather the mix of non-radiative and bimolecular recombination processes. This recombination mechanism may be attributed to the unbalanced injection of holes and electrons into the structure. The highest Z value (1.9) was obtained in the sample with 1.2 nm of cerium. This implies that bimolecular recombination could be dominant. The dependence of Z values on the thickness of cerium in the films varies similarly as an integral of EL intensity: the cerium doping increases the Z value, however, after reaching the excess amount it begins to decrease.

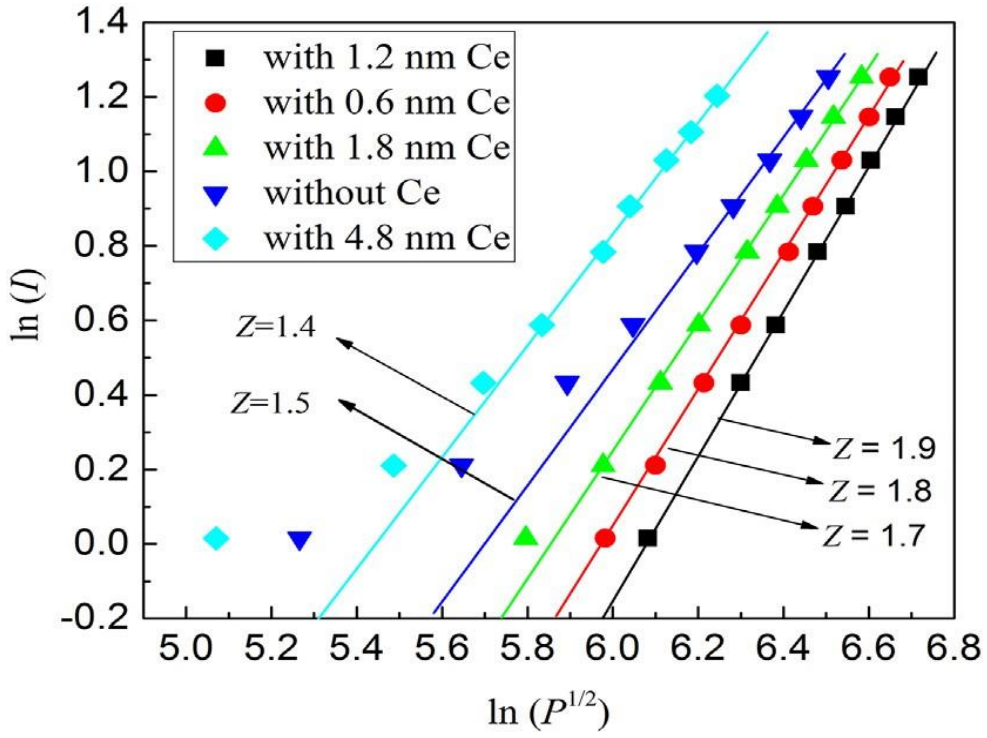

Fig. 7.8. ln(I) versus $\ln(P^{1/2})$ plot for the samples with the different thicknesses of cerium.

7.5 Degradation of Ce:SiN_x layers

The degradation of our device has been determined by measuring L-t curve at the constant density of current. The evolution of integral EL intensity is shown in the Fig. 7.9. The EL intensity demonstrates rapid initial decay and a moderate decrease in the long time region. This trend could be fitted by a sum of a two different exponential decay functions [44]:

$$\frac{L(t)}{L_0} = ae^{-\alpha t} + be^{-\beta t}; \qquad (7.4)$$

here a, b, α, β are the fitting parameters. This behaviour suggests that degradation of the structure is influenced by the multiple independent degradation mechanisms. The lifetime of the device (at a moment when EL intensity decreases by half) has been evaluated by extrapolation of the fitted function and is equal to 1200 h.

The electroforming effect is possible explanation of the initial rapid EL decrease of the device. The structural changes in the SiN_x films may be observed due to the Joule heating. Usually, the thermal breakdown is accompanied by nanocrystallization of the film, the increase of electroluminescence, the decrease of shunt resistance, or by the diffusion of metal from the electrodes into the film [10, 45]. The duration of electroforming process depends on the strength of the applied electric field and may vary from hours to a few seconds [10]. During EL degradation measurements the current density was fixed at 100 mA/cm^2. During the first 3 h the applied voltage monotonously dropped from 16.9 V to 15.3 V and stayed constant during the rest duration of experiment. The flow of current formed the permanent regions of lower

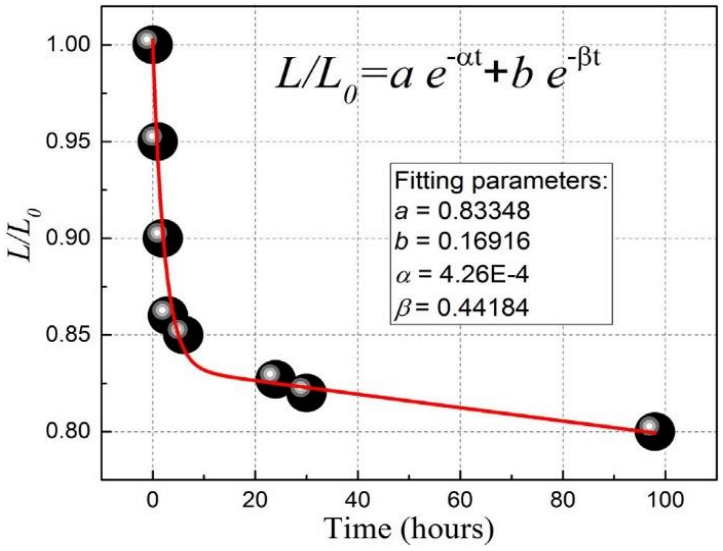

Fig. 7.9. L-t curve for $N_{1.2}$ sample. The current density was fixed at 100 mA/cm^2. Full circles shows the experimental data and a red line demonstrates fitting according to Eq. (7.4).

resistivity in the SiN_x sublayers. These structural changes may reduce the density of defect states and cause the decrease of EL intensity. Additionally, the incorporation of metal into the films may distort the local periodic field near the Ce^{3+} ions and weaken the EL.

In conclusion, the broad emission band at 650 nm is originated from an optically active defects in SiN_x lattice and the 460 nm band is attributed to the radiative transition from 5d–4f energy levels of Ce^{3+} ions. The transport of charge carriers is interpreted as Poole-Frenkel thermionic emission at high electric field and the dominant recombination mechanism depends on the level of cerium doping.

References

[1] R. J. Walters, G. I. Bourianoff and H. A. Atwater, *Field-effect electroluminescence in silicon nanocrystals*, Nat. Mater. **4** (2005) 143.

[2] J. Kramer, P. Seitz, E. F. Steigmeier, H. Auderset and H. Baltes, *Light-emitting devices in industrial CMOS technology*, Sensor. Actuat. A-phys. **37-38** (1993) 527.

[3] Z. Xie, D. J. Blackwood, *White electroluminescence from ITO/porous silicom junctions*, J. Lumin. **134** (2013) 67.

[4] G. R. Lin, Y. H. Pai, C. T. Lin and C. C. Chen, *Comparison on the electroluminescence of Si-rich SiN_x and SiO_x based light-emitting diodes*, Appl. Phys. Lett. **96** (2010) 263514.

[5] M. Wang, X. Huang, J. Xu, W. Li, Z. Liu, K. Chen, Observation of the size-dependent blueshifted electroluminescence from nanocrystalline Si fabricated by KrF excimer laser annealing of hydrogenated amorphous silicon/amorphous-SiNx:H superlattices, Appl. Phys. Lett. 72 (1998) 722.

[6] S. Kalem, Optical investigation of a-Si:H/a-SiN:H snperlattices, Phys. Rev. B 37 (1988) 88.

[7] W. Xiang, H. Rui, S. Chao, S. Jie, G. YanQing, Interface effects on the electroluminescence spectra in amorphous-Si/silicon oxynitride multilayer structures, Sci. China Phys. Mech. Astron. 55 (2012) 1194.

[8] R. Huang, H. Dong, D. Wang, K. Chen, H. Ding, X. Wang, W. Li, J. Xu, Z. Ma, Role of barrier layers in electroluminescence from SiN-based multilayer light-emitting devices, Appl. Phys. Lett. 92 (2008) 181106.

[9] B. Averboukh, R. Huber, K.W. Cheah, Y.R. Shen, G.G. Qin, Z.C. Ma, W.H. Zong, Luminescence studies of a Si/SiO_2 superlattice, J. Appl. Phys. 92 (2002) 3564.

[10] M. Anutgan, T. Anutgan, I. Atilgan, B. Katircioglu, Transport and luminescence phenomena in electroformed silicon nitride-based light emitting diode, Philos. Mag. 93 (2013) 3332.

[11] K.S. Cho, N.M. Park, T.Y. Kim, K.H. Kim, G.Y. Sung, J.H. Shin, High efficiency visible electroluminescence from silicon nanocrystals embedded in silicon nitride using a transparent doping layer, Appl. Phys. Lett. 86 (2005) 071909.

[12] J. Zhou, G.R. Chen, Y. Liu, J. Xu, T. Wang, N. Wan, Z.Y. Ma, W. Li, C. Song, K.J. Chen, Electroluminescent devices based on amorphous SiN/Si quantum dots/amorphous SiN sandwiched structures, Opt. Express 17 (2008) 156.

[13] M.J.F. Digonnet, Rare-earth Doped Fiber Lasers and Amplifiers, second ed. Marcel Dekker, New York, 2001.

[14] S. Cueff, C. Labbe, O. Jambois, Y. Berencen, A. Kanyon, B. Garrido, R. Rizk, Structural factors impacting carrier transport and electroluminescence from Si nanoclustersensitized Er ions, Opt. Express 20 (2012) 22490.

[15] J.M. Sun, W. Skorupa, T. Dekorsy, M. Helm, L. Rebohle, T. Gebel, Efficient ultraviolet electroluminescence from a Gd-implanted silicon metal-oxide-semiconductor device, Appl. Phys. Lett. 85 (2004) 3387.

[16] J.M. Sun, W. Skorupa, T. Dekorsy, M. Helm, L. Rebohle, T. Gebel, Bright green electroluminescence from Tb^{3+} in silicon metal-oxide-semiconductor devices, J. Appl. Phys. 97 (2005) 123513.

[17] P.R. Griffiths and J.A. de Haseth, *Fourier Transform Infrared Spectrometry*, 2nd ed. (John Wiley & Sons Inc., New Jersey, 2007).

[18] M.H. Brodsky, M. Cardona, and J.J. Cuomo, Infrared and Raman spectra of the silicon-hydrogen bonds in amorphous silicon prepared by glow discharge and sputtering, Phys. Rev. B **16**, 3556.
[19] G. Lucovsky, J. Yang, S.S. Chao, J.E. Tyler, and W. Czubatyj, Nitrogen-bonding environments in glow-discharge-deposited a-Si:H films, Phys. Rev. B **28**, 3234–3240 (1983).
[20] W.A. Lanford and M.J. Rand, The hydrogen content of plasma-deposited silicon nitride, J. Appl. Phys. **49**(4), 2473–2477 (1978).
[21] W.A.P. Claassen, W.G.J.N. Valkenburg, F.H.P.M. Hab raken, and Y. Tamminga, Characteri zation of plasma silicon nitride layers, J. Electrochem. Soc. **130**, 2419–24230 (1983).
[22] G.E. Jellison Jr., V.I. Merkulov, A.A. Puretzky, D.B. Geohegan, G. Eres, D.H. Lowndes, and J.B. Caughman, Characterization of thin-film amorphous semiconductors using spectroscopic ellipsometry, Thin Solid Films **377–378**, 68 (2000).
[23] E. Bustarret, M. Bensouda, M. Habrard, J. Bruyère, S. Poulin, and S. Gujrathi, Configurational statistics in *a*-$Si_xN_yH_z$ alloys: A quantitative bonding analysis, Phys. Rev. B **38**(12), 8171–8184 (1988).
[24] J.C. Tauc, *Optical Properties of Solids* (North-Hol11 land, Amsterdam, 1972).
[25] S.M. Sze, *Physics of Semiconductor Devices* (John Wiley & Sons Inc., New York, 1969).
[26] C. Kittel, Introduction to Solid State Physics, 8th ed., Ch. 7 (John Wiley & Sons Inc.. New York, 2005).
[27] A. Piccirillo and A.L. Gobbi, Physical-electri-cal properties of silicon nitride deposited by PECVD on III–V semiconductors, J. Electrochem. Soc. **137**, 3910 (1990).
[28] R. Huang, Z. Lin, Z. Lin, C. Song, X. Wang, Y. Guo, J. Song, Suppression of hole overflow and enhancement of light emission efficiency in Si quantum dots based silicon nitride light emitting diodes, IEEE J. Sel. Top. Quantum Electron. 20 (2014) 8200306.
[29] J. Robertson, Band offsets of wide-band-gap oxides and implications for future electronic devices, J. Vac. Sci. Technol. B 18 (2000) 1785.
[30] D.J. DiMaria, P.C. Arnett, Hole injection into silicon nitride: interface barrier energies by internal photoemission, Appl. Phys. Lett. 26 (1975) 711.
[31] R. Schlaf, H. Murata, Z.H. Kafafi, Work function measurements on indium tin oxide films, J. Electron. Spectrosc. Relat. Phenom. 120 (2001) 149.
[32] Z.H. Cen, T.P. Chen, L. Ding, Z. Liu, J.I. Wong, M. Yang, W.P. Goh, S. Fung, Influence of implantation dose on electroluminescence from Si-implanted silicon nitride thin films, Appl. Phys. A 104 (2010) 239.
[33] L. Brus, Luminescence of silicon materials: chains, sheets, nanocrystals, nanowires, microcrystals, and porous silicon, J. Phys. Chem. 98 (1994) 3575.
[34] J. Warga, R. Li, S.N. Basu, L. Dal Negro, Electroluminescence from silicon-rich nitride/ silicon superlattice structures, Appl. Phys. Lett. 93 (2008) 151116.
[35] S.V. Deshpande, E. Gulari, S.W. Brown, S.C. Rand, Optical properties of silicon nitride films deposited by hot filament chemical vapor deposition, J. Appl. Phys. 77 (1995) 6534.
[36] B. Kollmitzer, P. Hadley, Thermodynamic properties of separable square-wave potentials, Physica B 406 (2011) 4373.

[37] M. Wang, J. Huang, Z. Yuan, A. Anopchenko, D. Li, D. Yang, L. Pavesi, Light emission properties and mechanism of low-temperature prepared amorphous SiNX films. II. Defect states electroluminescence, J. Appl. Phys. 104 (2008) 083505.
[38] S.W. Brown, S.C. Rand, Opticali properties of silicon nitride films deposited by hot filament chemical vapor deposition, J. Appl. Phys. 77 (1995) 6534.
[39] S.A. Cabañas-Tay, L. Palacios-Huerta, J.A. Luna-López, M. Aceves-Mijares, S. Alcántara-Iniesta, S.A. Pérez-García, A. Morales-Sánchez, Analysis of the luminescent centers in silicon rich silicon nitride light-emitting capacitors, Semicond. Sci. Technol. 30 (2015) 065009.
[40] L. Li, S. Wang, G. Mu, X. Yin, K. Ou, L. Yi, A novel violent/blue light-emitting device based on $Ce_2Si_2O_7$, Sci. Rep. 5 (2015) 16659.
[41] C. Lv, C. Zhu, C. Wang, D. Li, X. Ma, D. Yang, Ultraviolet-visible electroluminescence from metal-oxide-semiconductor devices with CeO2 films on silicon, AIP Adv. 5 (2015) 037107.
[42] V. Pankratov, L. Grigorjeva, D. Millers, T. Chudoba, R. Fedyk, W. Lojkowski, Time-resolved luminescence characteristics of cerium doped YAG nanocrystals, Solid State Phenom. 128 (2007) 173.
[43] L.L. Goddard, S.R. Bank, M.A. Wistey, H.B. Yuen, Z. Rao, J.S. Harris Jr., Recombination, gain, band structure, efficiency, and reliability of 1.5-μm GaInNAsSb/GaAs lasers, J. Appl. Phys. 97 (2005) 083101.
[44] C. Féry, B. Racine, D. Vaufrey, H. Doyeux, S. Cinà, Physical mechanism responsible for the stretched exponential decay behavior of aging organic light-emitting diodes, Appl. Phys. Lett. 87 (2005) 213502.
[45] M. Anutgan, T. Anutgan, I. Atilgan, B. Katircioglu, Electroforming of amorphous silicon nitride heterojunction pin visible light emitter, Trans. Electron. Devices 58 (2011) 2537.

List of publications related to the thesis:

Papers:

S1. T. Grigaitis, A. Naujokaitis, S. Tumėnas, G. Juška, and K. Arlauskas, *Characterization of silicon nitride layers deposited in three-electrode plasma-enhanced CVD chamber,* Lith. J. Phys. **55** (2015) 35–43.

S2. T. Grigaitis, A. Naujokaitis, G. Juška and K. Arlauskas, *Influence of sublayer thickness on electroluminescence from a-Si:H/SiNx superlattice structures*, Thin Solid Films 585 (2015) 20.

S3. T. Grigaitis, A. Naujokaitis, V. Sabonis, and K. Arlaukas, *Electroluminescence from SiNx layers doped with Ce3+ ions*, Thin Solid Films 622 (2017) 142.

Presentations at the conferences:

K1. T. Grigaitis, K. Arlauskas, Optical, electrical and morphological properties of silicon nitride (SiN_x:H) grown on different surfaces, EMRS 2013 Spring meeting, Strasbourg, France.

K2. T. Grigaitis, K. Arlauskas, Optical and electrical properties of doped variable band gap SiN_x:H, 21st International Conference on Materials and Technology 2013, Portorož, Slovenia

K3. T.Grigaitis, A. Naujokaitis, G. Juška, K. Arlauskas, Electroluminescence from silicon nitride/silicon superlattice structures, EMRS 2014 Fall meeting, Warsaw, Poland.

Author's contribution

The author of this thesis constructed a three-electrode chemical vapor deposition chamber, deposited SiN_x layers as well as a-Si/SiN_x and Ce:SiN_x electroluminescent structures. The author also carried out the electroluminescence and part of other optical measurements. The author was a leading author of the papers, which is the base of this dissertation, made presentations in the conferences.

Spectroscopic ellipsometry measurement were performed by dr. Saulius Tumėnas (Center for Physical Science and Technology, Department of Optoelectronics, Vilnius). The laser annealing was carried out in cooperation with Altechna R&D laboratory. Electron microscopy measurements were made by Arnas Naujokaitis (Center for Physical Science and Technology, Department of materials structure, Vilnius). Atomic force microscopy measurements were made by Giedrius Juška (Department of Solid State Electronics, Vilnius University).

Information about the author:

Name, Surname: Tomas Grigaitis

Birth date: 1985.09.05

Phone and email: +37068313830, tomasgrigaitis@gmail.com

Education: 2004 – 2008 Bachelor (Physics, Vilnius University),

2008 – 2010 Master (Modern Technology Physics and Management, Vilnius University),

2010 – 2016 Doctoral studies (Vilnius University).

Work experience: (2009 – 2016) Senior Engineer (Vilnius University),

(2016 – now) Junior Researcher (Vilnius University).